The melting curve of Ni to 1 Mbar

Oliver T. Lord, Ian G. Wood, David P. Dobson, Lidunka Vočadlo, Weiwei Wang, Andrew R. Thomson, Elizabeth T.H. Wann, Guillaume Morard, Mohamed Mezouar, Michael J. Walter

The melting curve of Ni to 1 Mbar

OLIVER T. LORD[a,*], IAN G. WOOD[a], DAVID P. DOBSON[a], LIDUNKA VOČADLO[a], WEIWEI WANG[b], ANDREW R. THOMSON[b], ELIZABETH T. H. WANN[a], GUILLAUME MORARD[c], MOHAMED MEZOUAR[d], MICHAEL J. WALTER[b]

[a]Department of Earth Sciences, University College London, Gower Street, London, WC1E 6BT, UK

[b]School of Earth Sciences, University of Bristol, Wills Memorial Building, Queen's Road, Bristol, BS8 1RJ, UK

[c]Institut de Minéralogie, de Physique des Matériaux, et de Cosmochimie (IMPMC)
Sorbonne Universités - UPMC Univ Paris 06, UMR CNRS 7590, Muséum National d'Histoire Naturelle, IRD UMR 206, 4 Place Jussieu, F-75005 Paris, France.

[d]European Synchrotron Radiation Facility, BP 220, F-38043 Grenoble Cedex, France.

*Corresponding Author

Email: Oliver.Lord@bristol.ac.uk

Phone: +44 117 9545421

Fax: +44 117 9253385

Total number of words in Main text: 6491

Abstract: 293

Number of tables: 1

Number of figures: 7

References: 68

Abstract

The melting curve of Ni has been determined to 125 GPa using laser-heated diamond anvil cell (LH-DAC) experiments in which two melting criteria were used: firstly, the appearance of liquid diffuse scattering (LDS) during *in situ* X-ray diffraction (XRD) and secondly, plateaux in temperature vs. laser power functions in both *in situ* and off-line experiments. Our new melting curve, defined by a Simon-Glatzel fit to the data where $T_M\,(K) = [\left(\frac{P_M}{18.78\pm10.20} + 1\right)]^{1/2.42\pm0.66} \times 1726$, is in good agreement with the majority of the theoretical studies on Ni melting and matches closely the available shock wave melting data. It is however dramatically steeper than the previous off-line LH-DAC studies in which determination of melting was based on the visual observation of motion aided by the laser speckle method. We estimate the melting point (T_M) of Ni at the inner-core boundary (ICB) pressure of 330 GPa to be $T_M = 5800 \pm 700$ K (2σ), within error of the value for Fe of $T_M = 6230 \pm 500$ K determined in a recent *in situ* LH-DAC study by similar methods to those employed here. This similarity suggests that the alloying of 5-10 wt.% Ni with the Fe-rich core alloy is unlikely to have any significant effect on the temperature of the ICB, though this is dependent on the details of the topology of the Fe-Ni binary phase diagram at core pressures. Our melting temperature for Ni at 330 GPa is ~2500 K higher than that found in previous experimental studies employing the laser speckle method. We find that those earlier melting curves coincide with the onset of rapid sub-solidus recrystallization, suggesting that visual observations of motion may have misinterpreted dynamic recrystallization as convective motion of a melt. This finding has significant implications for our understanding of the high-pressure melting behaviour of a number of other transition metals.

23 **Keywords**

24 Nickel; melting; laser-heated diamond anvil cell; high-pressure

1. Introduction

The inner core of the Earth is perpetually solidifying at the expense of the overlying liquid outer core as the Earth undergoes secular cooling over geological time. The boundary between these two regions (the inner core boundary or ICB) is, by definition, close to the *P-T* condition at which the geotherm intersects the solidus of the Fe-rich core alloy. An accurate knowledge of this solidus at the ICB pressure of 330 GPa would provide an anchor for the construction of an accurate geotherm, which would in turn allow us to model more accurately the thermal and chemical structure of the Earth's core, and by extension, the overlying mantle.

Attempts to estimate the solidus of the core alloy at 330 GPa are complicated by the fact that the composition of the core alloy is itself poorly constrained and the subject of on-going research (e.g.: Fischer et al., 2013; Antonangeli et al., 2010; Aitta, 2010). However, an upper bound is provided by the melting temperature of pure Fe, given that Fe is the dominant component of the core. Although a broad range of techniques have been applied to this end, the resulting estimates for this upper bound on the ICB temperature (T_{ICB}) were, until recently, highly contradictory, spanning nearly 3000 K. The lowest published estimate is that of Boehler (1993) at 4850±200 K. This is based on a melting curve for Fe determined from visual observations of motion, interpreted as convection in a melt, up to 200 GPa in the laser-heated diamond anvil cell (LH-DAC). The highest estimate is that of Williams et al. (1987), who estimated a temperature of 7600±500 K by combining similar measurements in the LH-DAC with data from the earlier shock experiments of Brown & McQueen (1986) in which the melting temperature was determined from discontinuous changes in the sound velocity of a shocked Fe sample.

More recently, a consensus has begun to emerge toward the hot end of this range. The most recent *ab initio* molecular dynamics (MD) simulations, based on density functional theory (DFT) lead to an estimate of 6370±100 K (Alfè, 2009) while the state-of-the-art quantum Monte Carlo (QMC) simulations of Sola & Alfè (2009) give 6900±400 K. Both of these estimates compare

50 favourably with the value of 6230±500 K extrapolated from the melting curve of Anzellini et al.
51 (2013) which was determined solely on the basis of the appearance of liquid diffuse scattering
52 (LDS) during *in situ* synchrotron X-ray diffraction (XRD) measurements in the LH-DAC. The
53 shock data of Nguyen & Holmes (2004) fall close to this new curve, as does the original point
54 determined by Brown & McQueen (1986). Additionally, novel methods such as the shock melting
55 of pre-heated samples (Ahrens et al., 2002) and the detection of melting by the monitoring of
56 changes in the mean-square displacement of the Fe atom either by nuclear resonant inelastic X-ray
57 scattering (Murphy et al., 2011) or synchrotron Mössbauer spectroscopy in the LH-DAC (Jackson
58 et al., 2013) yield slightly shallower melting curves and thus somewhat lower values of T_{ICB} of
59 ~5700 K that are nevertheless within mutual error of the estimates based on the more traditional
60 methods previously described. These marginally shallower slopes are in good agreement with the
61 most recent shock melting data (Sun et al., 2005; Tan et al., 2005) as well as earlier *in situ* XRD
62 measurements in the LH-DAC (Ma et al., 2004; Shen et al., 2004; 1998). A more detailed
63 discussion of the Fe melting literature can be found in Anzellini et al. (2013).

64 Regardless of this apparent consensus, these estimates represent upper bounds on T_{ICB} that
65 will be revised downwards as the effects of alloying elements are included. The relevant alloying
66 elements that must be considered are Ni, of which there may be 5-10 wt.% in Earth's core, and one
67 or more elements lighter than Fe. The most likely candidates are some subset of Si, O, C, S and H
68 (Aitta, 2010; McDonough, 2004; Allègre, 1995), required to explain the density of both the inner
69 and outer core as determined from seismic studies (Dewaele et al., 2006; Yamazaki et al., 2012;
70 Garai et al., 2011). It is the effect of Ni that is the subject of this study.

71 The addition of Ni has the potential to reduce T_{ICB} considerably because its experimentally
72 determined melting curves, to date, are very much lower than that of pure Fe: when extrapolated to
73 330 GPa, the melting curve proposed by Lazor et al. (1993) and that based on the combined datasets
74 of Errandonea et al. (2013; 2001) and Japel et al. (2005) yield melting temperatures of 3300 K and

3200 K respectively which are 2400-3700 K lower than the range of Fe melting temperatures described above (Fig. 1). Many topologies are possible for the liquidus in the Fe-Ni system, and on the basis of the subsolidus phase relations of Kuwayama et al. (2008) and Tateno et al. (2012), two likely alternatives are shown in Supplementary Figure 1. Assuming melting temperatures of 6230 K for Fe (Anzellini et al., 2013) and 3300 K for Ni (Lazor et al., 1993), a simple linear interpolation indicates that 10 wt.% Ni in the bulk core alloy could reduce the melting temperature by ~300 K. But the depression might be much greater, especially for a topology like that shown in SF1b. Thus, on the basis of the current data for melting of Ni at high pressures, a large melting point depression might be the expectation in the Fe-Ni system.

However, as Fig. 1 illustrates, this conclusion suffers from a significant problem: although the existing experimentally determined melting curves for Ni agree closely with one another, there is a very considerable mismatch between these experimental curves and those determined from MD simulations. These have much steeper melting slopes than their LH-DAC experimental counterparts and consequently much higher Ni melting points at 330 GPa: simulations using classical potentials give 5300 K (Bhattacharya et al., 2011), 5900 K (Koči et al., 2006), 6700 K (Weingarten et al., 2009), 6800 K (Zhang et al., 2014b) and 10,000 K (Luo et al., 2010) while extrapolating the only DFT based *ab initio* study gives 6700 K (Pozzo & Alfè, 2013). The available shock melting data for Ni fall in the middle of this spread of MD melting curves (Fig. 1; Urlin et al., 1966). Although there is huge variation between these MD values, even the lowest (that of Bhattacharya et al., 2011) is ~2000 K higher than the estimates based on the LH-DAC experiments. The absolute reduction in T_{ICB} due to the mixing of Ni with Fe is dependent on the detailed topology of the Fe-Ni system at 330 GPa and it is formally impossible to determine its magnitude from the melting points of the end-members alone. Nonetheless, if these MD melting curves are correct, then for any given topology of the Fe-Ni system, the reduction in T_{ICB} is likely to be significantly smaller than would be expected on the basis of the existing experimental Ni melting curves (Fig. S1). Thus, the

accuracy of any estimate of T_{ICB} (and more generally, the accuracy of any Fe-Ni binary phase diagram at inner core pressures) is strongly dependent upon which of the published melting curves of Ni is correct.

The present study is primarily concerned with the geophysical implications of the melting curve of Ni. However, an additional motivation concerns the high-pressure melting behaviour of the transition metals in general. The striking dissimilarity between the shallow slopes of melting curves determined in LH-DAC experiments and the much steeper slopes determined from MD simulations is not unique to Ni, but is a well-established feature seen in a range of transition metals including Mo, Ta and W (e.g.: Errandonea, 2005). As is the case with Ni, the results of shock melting experiments on these elements (Mo: Nguyen et al., 2014; Hixson et al., 1989; Ta: Brown & Shaner, 1983; W: Hixson & Fritz, 1982) yield temperatures that are much closer to the MD simulations than to the static LH-DAC experiments. This has led to postulated phase diagrams that contain additional high-pressure phases designed to bring the LH-DAC experiments ($P \leq 100$ GPa; e.g. Errandonea et al., 2001) and high pressure shock experiments (P < 200 GPa; Nguyen et al., 2014; Hixson et al., 1989) into agreement (e.g.: Errandonea et al., 2005; Wu et al., 2009; Ross et al., 2007a; 2007b). However, these hypotheses fail to explain the huge disparities between the MD simulations (e.g. Cazorla et al., 2007) and shock experiments performed at lower pressures (Zhang et al., 2008) on the one hand and the static LH-DAC experiments on the other at $P \leq 100$ GPa.

An alternative explanation for the discrepancy is that the static LH-DAC melting experiments, in which visual observations of melt motion were used as the primary melting criterion, are not correct. A recent study by Dewaele et al. (2010), in which the melting curve of Ta was determined from the appearance of LDS during *in situ* XRD in the LH-DAC, found a much steeper melting curve than the earlier LH-DAC studies (Errandonea et al., 2003; 2001) and one that is in reasonable agreement with the MD simulations (Taioli et al., 2007; Liu et al., 2008). This situation is qualitatively similar to the Fe melting curve, in which static melting determinations

125 based on the appearance of LDS (Anzellini et al., 2013) agree well with the MD simulations (Alfè,
126 2009; Sola & Alfè, 2009) and shock measurements (e.g.: Nguyen & Holmes, 2004) but are
127 considerably higher than earlier melting curves determined in the LH-DAC using visual
128 observations of melt motion (Boehler, 1993). It seems plausible that what is apparent in Fe and Ta
129 may well turn out to be the case for other elements, such as W, Mo and Ni.

130 To determine which of the published Ni melting curves are correct, we have collected two
131 sets of melting data, both using the LH-DAC. The first set were performed *in situ* at beam line ID-
132 27 of the European Synchrotron Radiation Facility (ESRF) in Grenoble, France (§2.2). In these
133 experiments the appearance of LDS coupled with plateaux in temperature vs. laser power functions
134 were the melting criteria. The second set of measurements were performed off-line at the School of
135 Earth Sciences, University of Bristol (§2.3), in which the observation of plateaux in temperature vs.
136 laser power functions was the sole melting criterion (as described in §2.4 and by e.g. Lord et al.,
137 2014; 2010; 2009).

2. Methods

2.1 Sample assemblies

Pressure was generated using Princeton-type symmetric DACs with culets ranging from 250 μm to 150 μm in diameter (the latter bevelled at 8° out to a diameter of 250 μm). Rhenium, initially 250 μm thick was indented to a pressure of 25 GPa and drilled centrally to create a sample chamber ⅓ the diameter of the culet. Samples consisted of either ~5 μm thick densified foils made by compressing Ni powder between diamond anvils, or discs cut from 12.5 μm thick Ni sheet (both 99.95% purity; Goodfellow Cambridge Ltd.) using a UV laser ablation unit. The discs were then polished on both sides to a thickness of ~5 μm using 0.1 μm grade Al_2O_3 impregnated Mylar lapping film and then cleaned under acetone to remove any polishing debris.

Samples slightly smaller than the diameter of the sample chamber were loaded between form fitting discs of KCl or MgO, ~15 μm thick, that acted as both pressure medium and thermal insulation. These discs were cut, also using UV laser ablation, from sheets made by compressing powder in a hydraulic press. Pressure was monitored during compression (in all experiments) as well as before and after laser heating (in the off-line experiments) using the fluorescence of sub-micron grains of Cr:Al_2O_3 (ruby). In the off-line experiments, these grains were placed next to the sample and between the layers of pressure medium whereas in the *in situ* X-ray diffraction experiments (in which the ruby was not used to determine the pressure of the experiment) they were placed next to the sample chamber, between the gasket and the diamond anvil, to simplify the analysis of our XRD patterns. After loading, each cell was heated at 120°C for 1 hour under an argon atmosphere before being sealed under the same conditions to remove any water adsorbed during loading.

2.2 In situ experiments

Samples were laser-heated in a double-sided off-axis geometry with temperatures measured spectroradiometrically from the light collected using reflective optics from a 2 × 2 μm area centred on the 20-30 μm diameter laser-heated spot. Before the start of XRD, temperatures were measured on both sides and were equalized by varying the power of the lasers; during XRD, temperature was measured only on the upstream side, due to the need to remove the temperature-measuring optics from the path of the diffracted X-rays on the downstream side. The laser power was increased incrementally and linearly with a 3 s dwell time at each power during which the detector was automatically exposed to the diffracted X-rays. Temperatures were measured continuously and as often as allowed by the acquisition time of the spectrometer, which varied inversely with temperature. Typical temperature steps are <100 K (Fig. 4a) and a complete heating cycle took 5-15 minutes to complete. For further details of the laser heating system see Schultz et al. (2005).

The X-ray beam (33 keV; λ = 0.3738 Å; FWHM = 3 μm) was co-aligned to the centre of the laser heated spot using the X-ray induced fluorescence of either the pressure medium or the Re gasket. Diffracted X-rays were collected with a MAR165 CCD detector calibrated for sample to detector distance using a LaB_6 standard. The resulting patterns, masked to remove saturated spots, were integrated into 1-D spectra using the Fit2D program (Hammersley, 1997) and fitted using the Le Bail method (Le Bail *et al.*, 1988) as implemented in the GSAS suite of programs (Larson & Von Dreele, 2000; Toby, 2001). Further details of the X-ray optics and beam-line design can be found in Mezouar et al. (2005).

Pressure was determined before and after each melting experiment from the measured unit-cell volume of the Ni sample using the Vinet equation of state (EOS) reported by Dewaele et al. (2008). During laser heating, the total pressure (P_M), including the thermal pressure component, P_{TH}, was determined from the sample volume and temperature using a Mie-Gruneisen-Debye thermal EOS. This EOS was determined by fitting the high temperature *P-V-T* data reported in

Table S3 of Campbell et al. (2009) while fixing $K_{0,300}$, $K'_{0,300}$ and $V_{0,300}$ at the values of 176.7 GPa, 5.23 and 10.942 Å^3 atom^{-1} respectively, reported by Dewaele et al. (2008). These parameters were chosen because they more accurately reproduce the room temperature *P-V* data reported in Table S3 of Campbell et al. (2009) than do the parameters reported in their Table 1. This fit gives $\gamma_0 = 2.48 \pm 0.03$, $q = 2.4 \pm 0.3$ and $\Theta_{D,0} = 415\ K$ (Knacke et al., 1991). In spite of this complication, the effect of the chosen thermal EOS on our results is modest; in our highest-pressure *in situ* experiment, the calculated pressure of melting at the melting temperature (T_M) of the sample is 77±2 GPa using our thermal EOS (described above) and 74±2 GPa if we use the EOS parameters reported in Campbell et al. (2009).

Melting was detected using two criteria: 1) the appearance of plateaux in temperature vs. laser power curves and 2) the appearance of LDS in the XRD patterns. In all experiments we define T_M as the average of the temperatures within the plateau in the temperature vs. laser power function rather than using the appearance of LDS, to make our *in situ* results directly comparable to our off-line data (§2.3). Because LDS was always observed after the onset of and within a temperature plateau, using the appearance of LDS to define T_M makes almost no difference to our reported values. Our reported uncertainties in T_M are calculated by combining the average of the analytical uncertainty in the temperature measurements used to calculate T_M (2-5 K) with their standard deviation (50-100 K). Similarly, P_M is defined as the average of the pressures determined from all the diffraction patterns collected during the plateau used to define T_M. The uncertainties in P_M are calculated in the same way, by combining the average of the uncertainties in the pressures used to determine P_M with their standard deviation. In both cases errors have been combined assuming that they are uncorrelated.

2.3 Off-line experiments

Samples were heated using the on-axis double-sided laser heating system in the School of Earth Sciences, University of Bristol, which is described in detail in a previous publication (Lord et al., 2014). Briefly, the system consists of two 100 W diode pumped TEM_{00} fibre lasers (λ = 1070 nm). Beam-shaping optics and variable beam expanders were employed in the laser path to produce a flat-topped temperature profile with a diameter of 10-30 μm at the sample surface. The power to the lasers was automatically increased linearly as a function of time, with a constant offset designed to equalize the initial temperature of the two sample surfaces.

In every experiment, temperature cross-sections were measured spectroradiometrically along a transect across the laser heated spot (simultaneously, on both sides) by fitting the Wien function to spatially resolved spectra of the emitted incandescent light (Walter & Koga, 2004). Details of this technique, the associated uncertainties and the results of ambient pressure calibration experiments are all described in detail elsewhere (Lord et al., 2014; 2010; 2009). In a few experiments, the 1-D spectroradiometric cross-sections were supplemented with 2-D temperature maps measured on the left hand side only using a newly installed multi-spectral imaging radiometry system, based on the design described in Campbell (2008). Briefly, this method involves the acquisition of images of the laser-heated spot at four different wavelengths (670, 750, 800 and 900 nm) on a single CCD camera. The four images are then spatially correlated, based on a calibration image of a backlit pinhole with a diameter of ~2-3 μm such that, at each pixel, four intensity-wavelength data points are available. Temperature and emissivity are then determined at the pixel of interest by fitting the grey-body Wien function to the combined data from a 9 × 9 pixel box centred on the pixel of interest (giving a total of 324 data points). This last step is done to smooth the measured temperatures to match the optical resolution of the temperature measurement system (~3 μm; Lord et al., 2014). These procedures are replicated for every pixel to give 2-D maps of temperature and emissivity. This method has several advantages over traditional 1-D apertured spectroradiometry.

First of all, because the entire hotspot is imaged, the peak temperature can always be determined. In spectroradiometry, any slight misalignment of the hot spot with the spectrometer aperture will lead to an underestimation of the peak sample temperature. This is especially true during melting experiments, where the hotspot may move rapidly. Secondly, because each of the images can be focused independently onto the CCD, imaging radiometry should lead to the complete removal of chromatic effects from the measured temperatures (Lord et al., 2014). Finally, imaging the entire temperature field potentially allows us to observe the dynamic changes in sample temperature and morphology that occur during melting which are only partially evident when using spectroradiometry. These changes may also form the basis of an additional corroborative melting criterion.

After quenching to room temperature, the fluorescence of the ruby closest to the location of melting was used to determine the melting pressure, using the calibration of Dewaele et al. (2008). The uncertainty in these measurements is obtained by combining three uncorrelated terms: one which encompasses the disagreement between the various recently published ruby scales available (to a maximum of ±3 GPa at 110 GPa; see Fig. 3 of Dewaele et al. 2008), a second (of ±0.5-1.0 GPa) to take account of radial pressure gradients and a third (±0.2 GPa) to take account of the error in determining the position of the R_1 fluorescence line. To determine P_M for the off-line experiments, these post-heating pressures have been corrected for the effects of thermal pressure as estimated from the *in situ* experiments in which the thermal pressure was measured directly (§2.5). Reported values of T_M and their uncertainties were determined as in the *in situ* experiments.

2.4 Melt detection

As described in §2.2, T_M was determined from the appearance of features, often plateaux, in the temperature vs. laser power functions recorded during both the *in situ* and off-line experiments. This was corroborated, in nearly every *in situ* experiment, by the appearance of LDS in the XRD

patterns; whenever this was the case, the LDS appeared at the same temperature as the plateau, though usually at a higher laser power.

For an in-depth discussion of the rationale behind the use of plateaux in laser power vs. temperature functions as a melting criterion, the reader is referred to Lord et al. (2014; 2010; 2009) and Thomson et al. (2014). In summary, we have successfully applied this technique to a range of materials, including Fe, Pt, Pb, FeS, Fe_3C, Fe_7C_3, the Fe-Fe_3C eutectic, FeSi, and NiSi and the solidi in the $MgCO_3$-$CaCO_3$ and $MgCO_3$-$MgSiO_3$ systems. In the case of FeSi, Fe_3C, Fe_7C_3, the Fe-Fe_3C eutectic and the eutectics in the $MgCO_3$-$CaCO_3$ and $MgCO_3$-$MgSiO_3$ systems, our melting curves are corroborated by the *ex situ* textural analysis of large volume press (LVP) experiments, where measurements overlap. More importantly, there are now several materials for which melting temperatures have been determined using this method and are found to be in excellent agreement with direct observations of melting from the appearance of LDS during *in situ* XRD. These include, but are not limited to, FeSi (plateaux: Lord et al., 2010; LDS: Fischer et al., 2013), $Fe_{85}Ni_5Si_{10}$ (plateaux: Lord et al., 2014; LDS: Morard et al., 2011) and $Fe_{91}Si_9$ (plateaux: Fischer et al., 2013 and Asanuma et al, 2010; LDS: Fischer et al., 2013 and Morard et al., 2011). Most important of all is the case of NiSi, in which LDS was observed to occur concurrently with plateaux in the temperature vs. laser power function (Lord et al., 2014).

2.5 Thermal pressure correction of off-line experiments

To allow our off-line and *in situ* melting data to be combined, we have corrected our off-line data to include the effects of P_{TH}. For these experiments, the relation $P_{TH} = \alpha K_T(T_m - T_0)$, which assumes that αK_T is a constant, does not accurately reproduce our measured values of P_{TH}. Instead, we have determined, by linear regression, the empirical relationship between $P_{TH} = P_M - P_{300}$ and P_{300} in our *in situ* experiments (where P_{300} is the pressure measured after quenching to room temperature). This relationship is presented in Fig. 2 for experiments in which the pressure medium

was MgO (filled circles) and KCl (open circles). In both cases the data indicate a linear correlation that is slightly positive, indicating that the magnitude of the thermal pressure will increase with increasing compression, as expected.

It is also clear that at any given value of P_{300}, P_{TH} is at least a factor of ~8 smaller when KCl, as opposed to MgO, is used as the pressure medium. This is not surprising because P_{TH} depends on the coefficient of thermal expansion of the sample and the compressibility of the pressure medium and KCl is significantly more compressible than MgO over the *P*-*T* range of the data.

The data in Fig. 2 relating to each pressure medium are fitted separately, with equal weights, to a straight line, giving $P_{TH} = 7.7(23) + 0.06(5)P_{300}$ for experiments in MgO and $P_{TH} = 0.03(1)P_{300}$ for experiments in KCl (in the latter case the y-intercept was set to 0 to prevent negative thermal pressures at $P < 10$ GPa). The value of P_M for each off-line experiment was then calculated as the sum of P_{TH}, calculated using the relations defined above, and P_{300}, determined after heating by ruby fluorescence spectroscopy. The uncertainties involved in this P_{TH} correction procedure are fully propagated through to the uncertainties on the reported values of P_M (Table 1).

3. Results

The corrected Ni melting data are presented in Fig. 3 while Table 1 contains the data both with and without correction for P_{TH}. It is clear that the off-line and *in situ* measurements (squares and circles in Fig. 3 respectively) are in excellent agreement with one another, as observed in a previous study on NiSi (Lord et al., 2014). The pressure medium used, either MgO or KCl, also has no significant effect on melting temperature. Our preferred melting curve for Ni (the thick black line in Fig. 3) is an equally weighted fit to all the data, corrected for thermal pressure, using the Simon-Glatzel equation (Simon & Glatzel, 1929), that yields $T_M = [\left(\frac{P_M}{18.78\pm10.20} + 1\right)]^{1/2.42\pm0.66} \times T_0$, where $T_0 = 1726$ K (the ambient pressure melting point of Ni; Weast et al., 1985). Extrapolating this fit to the ICB pressure of 330 GPa gives $T_M = 5800 \pm 700$ K (2σ). Fitting the uncorrected data in the same manner gives $T_M = [\left(\frac{P_M}{11.65\pm7.93} + 1\right)]^{1/2.82\pm0.89} \times T_0$ (the thin black line on Fig. 3) and yields an almost identical value of $T_M = 5700 \pm 900$ K (2σ) at the ICB, suggesting that the effects of thermal pressure and the correction applied to the off-line data has no substantive effect. It should be noted that both fits are highly anti-correlated, with coefficients of -0.99; thus the uncertainties on the two fitting parameters should not be considered independent.

Fig.4 shows an example of the *in situ* measurements in which MgO was used as the pressure medium. The sample temperature increases rapidly as a function of total laser power up to 2900 K at 27.8 % (Fig. 4a). At this point the temperature drops slightly and then rises again at a slower rate until remaining essentially constant from 32.2 % laser output until the end of the experiment. Averaging these temperatures (the filled circles) gives $T_M = 2820 \pm 90$ K. At 38.8 % output (marked by the arrow) LDS appears in the XRD patterns (Fig. 4b) and grows in intensity with increasing laser power until reaching a maximum at ~43 % laser output. As in our previous study on NiSi (Lord et al., 2014), we interpret the correlation between the plateaux in the temperature vs. laser power data and the LDS signal as confirmation that the generation of the plateau is directly

related to melting and is thus an accurate melting criterion. There are several possible reasons as to why the diffuse signal does not appear until after the onset of the plateau. Firstly, the diffuse signal may not be resolvable from the background until a sufficient melt volume is produced. Secondly, the melt may be mobile, making it hard to observe until the majority of the sample is melted at higher laser power; it is common for melted samples to exhibit holes after quenching, suggesting the melt has flowed away from the hotspot, and thus also away from the X-ray beam. Thirdly, this behaviour could be due to slight misalignments between the laser heated spot and the X-ray beam.

When MgO was used as the pressure medium, minor reaction between the mobile melt and the diamond anvils was evident in our *in situ* experiments. Fig. 5a shows a pattern collected at high temperature just before melting from experiment 65A; all the peaks can be indexed to fcc-Ni and MgO. After quenching (Fig. 5b), new, weak peaks appear that can be indexed using the cementite (Fe_3C) structure (space group *Pnma*), with a = 4.219(1) Å, b = 4.702(5) Å, c = 6.338(6) Å and V = 125.7(1) $Å^{-3}$. These values are very close to (but slightly smaller than) the values predicted for Fe_3C by Sata et al. (2010) at the post heating pressure of 56.1 GPa, suggesting that the trace phase is Ni_3C, which is a known metastable phase at 1 atm, albeit with a different, hexagonal, structure (Goto et al., 2008). An analysis of the relative areas of the Ni and Ni_3C peaks indicate that this phase represents a maximum of 13% of the sample by volume, which corresponds to a maximum C content of 0.55 wt. %. The effect of this minor contamination, which is hard to avoid, would be to reduce the measured melting temperature, assuming the Ni-C system is eutectic at these conditions, thus strengthening further the central conclusion of this paper that the Ni melting curve is hotter than previously thought. No such reaction products were observed after quench in the only *in situ* experiment in which KCl was used as the pressure medium (Fig. 5c).

Figs. 6 (experiment 77A at 28 GPa) and 7 (experiment 79B at 125 GPa) show examples of the *ex situ* data spanning the investigated pressure range. In the case of experiment 77A, the sample temperature was measured not only using spectroradiometry on both sides (the circles in Fig. 6a),

but also using multispectral imaging radiometry on the left hand side (the squares; see §2.3). Between the start of the experiment and a laser output of ~32 %, all three temperature measurements in experiment 77A are in close agreement (Fig. 6a) and the shape of the temperature field remains almost unchanged (compare Fig. 6b and c). This is because in the sub-solidus state, the variation in temperature is primarily a function of sample thickness. Nevertheless, the use of beam-shaping optics (see §2.3) means that the temperature variation within the ~20 μm diameter region on which the laser is incident (represented by the black circle in Fig. 6b) is no more than ±75 K. At ~32.5 % laser output, all three measurements register a sudden and transient increase in temperature. This is correlated with a dramatic change in the shape of the temperature field from a flat-topped Gaussian distribution to a toroidal distribution (Fig. 6d). This may be the result of a sudden ring shaped tear in the sample caused by melting, leading to a sudden increase in temperature in the thinned regions to ~2800 K, with a localized peak in the NW quadrant reaching ~3200 K. This behaviour is often, but not always observed; it likely depends on sample thickness and the strength of the pressure medium. It is not surprising that the spectroradiometric measurements underestimate the peak temperature at this point (see Fig. 6a); though the 1-D transect used for spectroradiometry (represented by the vertical bar in Fig. 6d) will almost certainly, as in this case, intersect the hot ring of the structure in Fig. 6d, it is very unlikely that a localized peak on that ring will happen to coincide with the aperture. As the laser power is increased further, all three measurements plateau while the shape of the temperature field recorded on the left hand side (Fig. 6f-j) changes considerably between every acquisition of data, behaviour that is indicative of the presence of a mobile melt (cf. Fig. 6b and c). The sudden change in the temperature distribution on melting also explains the increased disparity in peak temperature recorded by the three measurements within the melting plateau as compared to the initial temperature ramp (Fig. 6a). It is likely that on the right hand side (the filled circles in Fig. 6a) the aperture used for the spectroradiometric measurements happens to coincide with the location of the hottest part of the

sample surface, while the aperture on the left (the open circles) does not. It is this kind of misalignment between the rapidly moving melt and the 1-D spectroradiometric aperture that likely accounts for the fact that the scatter in the data in Fig. 3 (up to 300 K) is significantly larger than the formal error bars on the individual data points. In this case, the value of $T_M = 2620 \pm 70$ K was determined by averaging the right hand side spectroradiometric measurements and the multispectral imaging radiometry measurements made on the left hand side.

In the manner of Fischer & Campbell (2010) we looked for melting-related discontinuities in temperature vs. emissivity plots taken from our multispectral imaging radiometry data. However, we did not see any features that correlated consistently with our primary melting criterion. It is probable that such discontinuities, which Fischer & Campbell (2010) observed in melting experiments on wüstite ($Fe_{0.94}O$), depend on there being a change in the emissivity of the sample upon melting. The magnitude of this change will be material specific and perhaps is not large enough to be observable in Ni.

4. Discussion

4.1 Comparison with the literature

Over the range of the measurements (to 125 GPa) our new Ni melting curve is in excellent agreement with the majority of the MD studies of Ni melting: the *ab initio* study of Pozzo & Alfè (2013), and the studies of Weingarten et al. (2009) and Koči et al. (2006) which employed classical potentials. Indeed, the study of Luo et al. (2010), which also used classical potentials, is the only non-experimental study that significantly contradicts our new melting curve (1500 K hotter at 125 GPa). In addition to the MD simulations, the two shock melting points recalculated by Pozzo & Alfè (2013), on the basis of the equations of state of liquid and solid Ni reported by Urlin et al. (1966), fall almost exactly on our new melting curve.

However, our new Ni melting curve, along with all those determined on the basis of the theoretical and shock-wave data discussed above, diverges dramatically from the melting curves determined from the previous LH-DAC studies (Japel et al., 2005; Errandonea et al., 2001; Lazor et al., 1993). At 125 GPa, these curves are at least 1200 K below that reported here. This difference is most easily explained by the different melting criteria employed in the various studies. In all three of the previous LH-DAC studies, melting was determined on the basis of the observation of motion in the 'speckle' pattern created by a green Ar laser on the sample surface during laser heating (the laser speckle method), with the assumption being that such motion represented the convection of a liquid. However, the recent work of Anzellini et al. (2013) on Fe, in which melting was determined using the appearance of LDS during *in situ* XRD in the LH-DAC suggests an alternative explanation. They observed that an earlier (lower) melting curve (Boehler, 1993) that was determined using the laser speckle method, coincided with the onset of sub-solidus recrystallization as evidenced by the rapid change in the position of saturated spots around the Debye-Scherrer diffraction rings from the Fe sample. The supplementary video (S1) accompanying this paper shows the sequence of raw 2-D diffraction patterns collected during *in situ* run 65B at $P_M = 77.4 \pm 2.2$

GPa (see Table 1). At the start of the experiment, semi-continuous Debye-Scherrer rings can be seen from the Ni sample (the rings from the MgO pressure medium remain continuous throughout the experiment). At 2530 K, several large spots appear, associated with one of the Ni rings, indicative of the onset of rapid recrystallization; as the temperature rises, similar spots are present in nearly every pattern, but always in different locations around the Ni rings. In the pattern marked 3820 K toward the end of the video, a single, continuous diffuse ring, indicative of the presence of melt, appears suddenly. In this example, rapid recrystallization begins more than 1000 K before the first appearance of melt, which suggests that this commonly observed pre-melting phenomenon is not an accurate melting criterion. The open triangles on Fig. 3 represent the temperatures at which rapid recrystallization begins in all of the *in situ* experiments on pure Ni reported here. These temperatures correlate well with the earlier experimental melting curves determined in the LH-DAC using the laser speckle method, which suggests that those earlier studies on Ni, as is likely the case with Fe, were determining the temperature of sub-solidus recrystallization rather than melting. The new results further suggest that local structures in the liquid phase do not control the gradient of the Ni melting curve. Such local structures were proposed by Ross et al. (2007b) as a possible reason for the low gradient of the Ni melting curve as determined by the laser speckle method; in fact, their model from which the entropic effects of local liquid structure is removed matches well with our new melting data, the shock compression data, and the majority of the MD based simulations (cf. Fig. 3 from this paper with Fig. 4 of Ross et al. 2007b).

In contrast, the new Ni melting curve reported here is based on the direct observation of the presence of melt from its diffuse scattering signal during *in situ* XRD experiments, and the appearance of plateaux in temperature vs. laser power curves, which are themselves correlated with the appearance of LDS in the *in situ* experiments. The fact that our melting curve agrees closely with both the existing shock wave data and the majority of the computational studies gives us confidence in its accuracy.

437

438 *4.2 Implications for the phase diagrams of the transition metals*

439 The possibility that the laser speckle method may lead to the misidentification of sub-solidus
440 recrystallization as melting has considerable implications for many other transition metals for which
441 melting curves have been determined using this method. It is well known (Errandonea et al., 2005)
442 that the laser speckle studies on the bcc metals Mo, Ta and W define melting curves which are
443 much lower in temperature than those determined from MD simulations, shock wave experiments,
444 and in the case of Ta, *in situ* XRD in the LH-DAC where LDS was used as the melting criterion
445 (Dewaele et al., 2010). Co, Ti, V and Cr (Errandonea et al., 2001) have also been studied using the
446 laser speckle method, though less extensively by MD. Nevertheless, a recent MD study on Co
447 (Zhang et al., 2014a) yet again indicates a much steeper melting curve compared to the one
448 generated using the laser speckle method. In contrast, it is also apparent that the laser speckle
449 measurements on Al (Ross et al., 2004) and Cu, Pt and Pd (Errandonea et al., 2013) are in very
450 good agreement with the available shock wave and MD melting curves. We suggest that additional
451 studies should be performed on all of these metals, using the melting criteria employed in this
452 study, to determine whether the shallow slopes genuinely represent melting, and why the laser
453 speckle method appears to define melting accurately in some materials but not others.

454

455 *4.3 Implications for the temperature at the ICB*

456 Extrapolating our melting curve to the pressure of the ICB (330 GPa) yields $T_M = 5800 \pm$
457 700 K (2σ), which falls within error of the classical MD study of Koči et al. (2006; $T_M = 5950 \pm$
458 50 K) and the cell-theory based study of Bhattacharya et al. (2011; $T_M = 5330 \pm 50$ K). In
459 contrast, the only *ab initio* MD study of Ni melting (Pozzo & Alfè, 2013) predicts a value of
460 6740±180 K, nearly 1000 K higher. This value is however, like ours, an extrapolation, with
461 simulations having only been performed to 100 GPa, all of which give values within error of our

new melting curve. In contrast, the *ab initio* MD study of Fe by Alfè et al (2009), which used a similar method but was performed at 330 GPa, thus requiring no extrapolation, yields $T_M = 6400 \pm 100$ K which is very close to the value determined from the *in situ* LH-DAC experiments of Anzellini et al. (2013; $T_M = 6230 \pm 500$ K). It is apparent from the above (and Fig. 3) that the melting point of Ni at the ICB from this study and the value for Fe from the study of Anzellini et al. (2013), both of which rely on the appearance of LDS during *in situ* XRD, are within error of each other. This is also the case (albeit at a somewhat higher temperature) for the most recent *ab initio* MD studies on Ni (Pozzo & Alfè, 2013) and Fe (Alfè et al., 2009). This suggests that, regardless of which method is most accurate, Fe and Ni have very similar melting points at 330 GPa.

It is formally impossible to determine the melting point of an intermediate composition within a binary system from the melting points of the end-members alone. However, our new melting curve for Ni suggests that the reduction in T_{ICB} is likely to be significantly smaller than would be expected were the existing experimental Ni melting curves correct (Fig. S1), further bolstering claims that Earth's core is hotter than previously thought (Anzellini et al., 2013). To settle this question completely, full computational and experimental studies designed to determine the phase relations in the Fe-Ni binary system at core pressures are required. Nevertheless, our Ni melting curve adds a significant new constraint on those phase relations.

5. Conclusions

We have presented a new melting curve for Ni to 125 GPa, based on the appearance of LDS during *in situ* XRD in the LH-DAC and plateaux in temperature vs. laser power functions in both *in situ* and off-line experiments. The new melting curve is in excellent agreement with the majority of the theoretical (primarily MD) studies on Ni melting, and matches closely the available shock wave data. We estimate the melting temperature of Ni at the ICB pressure of 330 GPa as $T_M = 5800 \pm 700$ K (2σ), which is 2500 K higher than the value of $T_M \approx 3300$ K from the studies of Lazor et al. (1993), Japel et al. (2005) and Errandonea et al. (2013; 2001) which employed the laser speckle method as the melting criterion but close to the value of $T_M = 6230 \pm 500$ K for Fe from the recent study of Anzellini et al. (2013) as determined by methods comparable to those used here. Our new melting curve for Ni suggests that the reduction in T_{ICB} is likely to be significantly smaller than would be expected were the existing experimental Ni melting curves correct, further bolstering claims that Earth's core is hotter than previously thought (Anzellini et al., 2013).

Along with FeSi (Fischer et al., 2013) and NiSi (Lord et al., 2014), this study provides a further example of the accuracy as a melting criterion of plateaux in temperature vs. laser power functions because, in each case, melting temperatures determined in this way correlate exactly with direct observations of melting from the appearance of LDS during *in situ* XRD.

Analysis of our XRD patterns indicates that the earlier melting curves for Ni, determined by the laser speckle method, correlate with the onset of sub-solidus recrystallization rather than melting, as was observed in Fe (Anzellini et al., 2013). This has significant implications for a number of other transition metals, such as Mo, W, Co, V, Ti and Cr that also exhibit shallow melting slopes, but have thus far only been studied in the LH-DAC using the laser speckle method.

Finally, our 2-D temperature mapping, generated using multispectral imaging radiometry (Campbell, 2008) shows dramatic changes on melting in the dynamics of the temperature field that could be employed as a useful additional melting criterion in off-line LH-DAC studies.

Acknowledgements

This work was supported by the Natural Environment Research Council by grants awarded to LV at UCL (grant number NE/H003975/1), to MJW at Bristol (NE/H003541/1) and by a fellowship awarded to OTL at Bristol (NE/J018945/1) and by the PlanetLab program of the French National Research Agency by a grant awarded to GM (ANR-12-BS04-0015-04). We wish to thank Denis Andrault, Daniele Antonangeli and Julien Siebert for their generous help with both the preparation and running of in situ melting experiments at the ESRF.

512 **References**

513 Ahrens TJ, Holland KG, Chen GQ (2002) Phase diagram of iron, revised-core temperatures.
514 Geophys Res Lett 29 http://dx.doi.org/10.1029/2001GL014350
515 Aitta A (2010) The identity and quantity of the light matter on each side of the Earth's inner core
516 boundary. Phys Earth Planet Inter 181:132-140
517 Allègre CJ, Poirier J-P, Humler E, Hofmann AW (1995) The chemical composition of the Earth.
518 Earth Planet Sci Lett 134:515-526
519 Antonangeli D, Siebert J, Badro J, Farber DL, Fiquet G, Morard G, Ryerson FJ (2010) Composition
520 of the Earth's inner core from high-pressure sound velocity measurements in Fe–Ni–Si
521 alloys. Earth Planet Sci Lett 295:292–296
522 Anzellini S, Dewaele A, Mezouar M, Loubeyre P, Morard G (2013) Melting of Iron at Earth's
523 Inner Core Boundary Based on Fast X-ray Diffraction. Science 340:464-466
524 Asanuma H, Ohtani E, Sakai T, Terasaki H, Kamada S, Kondo T, Kikegawa T (2010) Melting of
525 iron–silicon alloy up to the core–mantle boundary pressure: implications to the thermal
526 structure of the Earth's core. Phys Chem Min 37:353-359
527 Bhattacharya C, Srivastava MK, Menon SVG (2011) Melting curves of FCC-metals by cell-theory.
528 Physica B 406:4035-4040
529 Boehler R, Ross M, Boercker DB (1996) High-pressure melting curves of alkali halides. Phys Rev
530 B 53:556-563
531 Boehler R (1993) Temperatures in the Earth's core from melting-point measurements of iron at
532 high static pressures. Nature 363:534-536.
533 Brown JM, McQueen RG (1986) Phase transitions, Grüneisen parameter, and elasticity for shocked
534 iron between 77 GPa and 400 GPa. J. Geophys. Res. 91:7485-7494

Brown JM, Shaner JW (1983) Rarefaction velocities in shocked tantalum and the high pressure melting point. In: Asay JR, Graham RA, Straub GA (Eds.) Shock Waves in Condensed Matter. Elsevier Science, New York

Campbell AJ, Danielson L, Righter K, Seagle CT, Wang Y, Prakapenka VB (2009) High pressure effects on the iron–iron oxide and nickel–nickel oxide oxygen fugacity buffers. Earth Planet Sci Lett 286:556-564

Campbell AJ (2008) Measurement of temperature distributions across laser heated samples by multispectral imaging radiometry. Rev Sci Instruments 79:015108

Cazorla C, Gillan MJ, Taioli S, Alfè D (2007) *Ab initio* melting curve of molybdenum by the phase coexistence method. J Chem Phys 126:194502

Dewaele A, Belonoshko AB, Garbarino G, Occelli F, Bouvier P, Hanfland M, Mezouar M (2012) High-pressure–high-temperature equation of state of KCl and KBr. Phys Rev B 85:214105

Dewaele A, Mezouar M, Guignot N, Loubeyre P (2010) High Melting Points of Tantalum in a Laser-Heated Diamond Anvil Cell. Phys Rev L 104:255701

Dewaele A, Torrent M, Loubeyre P, Mezouar M (2008) Compression curves of transition metals in the Mbar range: Experiments and projector augmented-wave calculations. Phys Rev B 78:104102

Dewaele A, Loubeyre P, Occelli F, Mezouar M, Dorogokupets PI, Torrent M (2006) Quasihydrostatic Equation of State of Iron above 2 Mbar. Phys Rev Lett 97:215504

Dorogokupets PI, Dewaele A (2007) Equations of state of MgO, Au, Pt, NaCl-B1, and NaCl-B2: Internally consistent high-temperature pressure scales. High Pressure Res 27:431-446

Errandonea, D (2013) High-pressure melting curves of the transition metals Cu, Ni, Pd, and Pt. Phys Rev B 87:054108

Errandonea D (2005) Improving the understanding of the melting behaviour of Mo, Ta, and W at extreme pressures. Physica B 357:356-364

560 Errandonea D, Somayazulu M, Häusermann D, Mao HK (2003) Melting of tantalum at high
561 pressure determined by angle dispersive x-ray diffraction in a double-sided laser-heated
562 diamond-anvil cell. J Phys Condens Matter 15:7635-7649
563 Errandonea D, Schwager B, Ditz R, Gessmann C, Boehler R, Ross M (2001) Systematics of
564 transition-metal melting. Phys Rev B 63:132104
565 Fischer RA, Campbell AJ, Reaman DM, Miller NA, Heinz DL, Dera P, Prakapenka VB (2013)
566 Phase relations in the Fe–FeSi system at high pressures and temperatures. Earth Planet Sci
567 Lett 373:54-64
568 Fischer RA, Campbell AJ (2010) High-pressure melting of wüstite. Am Min 95:1473-1477
569 Garai J, Chen J, Telekes G (2011) PVT equation of state of epsilon iron and its densities at inner
570 core conditions. Am Min 96:828-832
571 Goto Y, Taniguchi K, Omata T, Otsuka-Yao-Matsuo S, Ohashi N, Ueda S, Yoshikawa H,
572 Yamashita Y, Oohashi H, Kobayashi K (2008) Formation of Ni3C Nanocrystals by
573 Thermolysis of Nickel Acetylacetonate in Oleylamine: Characterization Using Hard X-ray
574 Photoelectron Spectroscopy. Chem Matter 20:4156-4160.
575 Hixson RS, Boness DA, Shaner JW, Moriarty JA (1989) Acoustic velocities and phase transitions
576 in molybdenum under strong shock compression. Phys Rev L 62:637-640
577 Hixson RS, Fritz JN (1992) Chock compression of tungsten and molybdenum. J Appl Phys 71:
578 1721-1728
579 Jackson JM, Sturhahn W, Lerche M, Zhao J, Toellner TS, Ercan Alp E, Sinogeikin SV, Bass JD,
580 Murphy CA, Wicks JK (2013) Melting of compressed iron by monitoring atomic dynamics.
581 Earth Planet Sci Lett 363:143-150
582 Japel S, Schwager B, Boehler R, Ross M (2005) Melting of copper and nickel at high Pressure: The
583 role of *d* electrons. Phys Rev Lett 95:167801

584 Knacke O, Kubaschewski O, Hesselmann K (1991) Thermochemical Properties of Inorganic
585 Substances, 2nd edition. Springer-Verlag, Berlin.
586 Hammersley AP (1997) FIT2D: an introduction and overview. ESRF Technical Report ESRF-97-
587 HA-02T, Grenoble, France
588 Koči L, Bringa EM, Ivanov DS, Hawreliak J, McNaney J, Higginbotham A, Zhigilei LV,
589 Belonoshko AB, Remington BA, Ahuja R (2006) Simulation of shock-induced melting of
590 Ni using MD coupled to a two-temperature model. Phys Rev B 74:012101
591 Kuwayama Y, Hirose K, Sata N, Ohishi Y (2008) Phase relations of iron and iron–nickel alloys up
592 to 300 GPa: Implications for composition and structure of the Earth's inner core. Earth
593 Planet Sci Lett 273:379-385
594 Larson AC, Von Dreele RB (1994) General Structure Analysis System (GSAS). Los Alamos
595 National Laboratory Report LAUR 86-748
596 Lazor P, Shen G, Saxena SK (1993) Laser-Heated Diamond Anvil Cell Experiments at High
597 Pressure: Melting Curve of Nickel up to 700 kbar. Phys Chem Minerals 20:86-90
598 Le Bail A, Duroy H, Fourquet JL (1988) Ab-initio structure determination of $LiSbWO_6$ by X-ray
599 powder diffraction. Mater Res Bull 23:447-452
600 Lord OT, Wann ETH, Hunt SA, Walker AM, Santangelli J, Walter MJ, Dobson DP, Wood IG,
601 Vočadlo L, Morard G, Mezouar M (2014) The NiSi melting curve to 70 GPa. Phys Earth
602 Planet Inter 233:13-23 http://dx.doi.org/10.1016/j.pepi.2014.05.005
603 Lord OT, Walter MJ, Dobson DP, Armstrong L, Clark SM, Kleppe A (2010) The FeSi phase
604 diagram to 150 GPa. J Geophys Res 115:B06208
605 Lord OT, Walter MJ, Dasgupta R, Walker D, Clark SM (2009) Melting in the Fe–C system to 70
606 GPa. Earth Planet Sci Lett 284:157-167
607 Lindholm M, Sundman B (1996) A thermodynamic evaluation of the nickel-silicon system. Met
608 Mat Trans A 27:2897-2903

609 Liu Z-L, Zhang X-L, Cai L-C, Chen X-R, Wu Q, Jing F-Q (2008) Thermal equation of state, and
610 melting and thermoelastic properties of bcc tantalum from MD. J Phys Chem Solids
611 69:2833-2840
612 Luo F, Chen X-R, Cai L-C, Ji G-F (2010) Solid-Liquid Interfacial Energy and Melting Properties of
613 Nickel under Pressure from MD. J Chem Eng Data 55:5149-5155
614 Ma Y, Somayazulu M, Shen G, Mao HK, Shu J, Hemley RJ (2004) In Situ X-ray Diffraction
615 studies of iron to Earth-core conditions. Phys Earth Planet Inter 143-144:455-467
616 McDonough WF (2003) Compositional Model for the Earth's Core. In: Carlson RW (Ed.), The
617 Mantle and Core. Elsevier-Pergammon, Oxford.
618 Mezouar M, Crichton WA, Bauchau S, Thurel F, Witsch H, Torrecillas F, Blattman G, Marion P,
619 Dabin Y, Chevanne J, Hignette O, Morawe C, Borel C (2005) Development of a new state-
620 of-the-art beamline optimized for monochromatic single-crystal and powder X-ray
621 diffraction under extreme conditions at the ESRF. J Synchrotron Radiation 12:659-664
622 Morard G, Andrault D, Guignot N, Siebert J, Garbarino G, Antonangeli D (2011) Melting of Fe–
623 Ni–Si and Fe–Ni–S alloys at megabar pressures: implications for the core–mantle boundary
624 temperature. Phys Chem Min 38:767-776
625 Murphy CA, Jackson JM, Sturhahn W, Chen B (2011) Melting and thermal pressure of hcp-Fe from
626 the phonon density of states. Phys Earth Planet Inter 188
627 http://dx.doi.org/10.1016/j.pepi.2011.07.001
628 Nguyen JH, Akin MC, Chau R, Fratanduono DE, Ambrose WP, Fat'yanov OV, Asimow PD,
629 Holmes NC (2014) Molybdenum sound velocity and shear modulus softening under shock
630 compression. Phys Rev B 89:174109
631 Pozzo M, Alfè D (2013) Melting curve of face-centered-cubic nickel from first-principles
632 calculations. Phys Rev B 88:024111

633 Ross M, Errandonea D, Boehler R (2007a) Melting of transition metals at high pressure and the
634 influence of liquid frustration: The early metals Ta and Mo. Phys Rev B 76:184118
635 Ross M, Boehler R, Errandonea D (2007b) Melting of transition metals at high pressure and the
636 influence of liquid frustration: The late metals Cu, Ni and Fe. Phys Rev B 76:184117
637 Ross M, Yang LH, Boehler R (2004) Melting of aluminium, molybdenum, and the light actinides.
638 Phys Rev B 70:184112
639 Sata N, Hirose K, Shen G, Nakajima Y, Ohishi Y, Hirao N (2010) Compression of FeSi, Fe_3C,
640 $Fe_{0.95}O$ and FeS under the core pressures and implication for light element in the Earth's
641 core. J Geophys Res 115:B09204, doi:10.1029/2009JB006975.
642 Schultz E, Mezouar M, Crichton W, Bauchau S, Blattmann G, Andrault D, Fiquet G, Boehler R,
643 Rambert N, Sitaud B, Loubeyre P (2005) Double-sided laser heating system for *in situ* high
644 pressure–high temperature monochromatic X-ray diffraction at the ESRF. High Pressure
645 Res. doi: 10 1080/08987950500076031
646 Shen G, Prakapenka VB, Rivers ML, Sutton SR (2004) Structure of Liquid Iron at Pressures up to
647 58 GPa. Phys Rev Lett 92:185701
648 Shen G, Mao HK, Hemley RJ, Duffy TS, Rivers ML (1998) Melting and crystal structure of iron at
649 high pressures and temperatures. Geophys Res Lett 25:373-376
650 Sola E, Alfè D (2009) Melting of iron under Earth's core conditions from diffusion Monte Carlo
651 free energy calculations. Phys Rev Lett 103:078501
652 Sun YH, Huang HJ, Liu FS, Yang MX, Jing FQ (2005) A direct comparison between static and
653 dynamic melting temperature determinations below 100 GPa. Chin Phys Lett 22:2002–2004
654 Taioli S, Cazorla C, Gillan MJ, Alfè D (2007) Melting curve of tantalum from first principles. Phys
655 Rev B 75:214103
656 Tan H, Dai CD, Zhang LY, Xu CH (2005) Method to determine the melting temperatures of metals
657 under megabar shock pressures. Appl Phys Lett 87:221905

658 Tateno S, Hirose K, Ohishi Y, Tatsumi Y (2010) The structure of iron in Earth's inner core. Science
659 330:359-361
660 Thomson A, Walter MJ, Lord OT, Kohn SC (in press) Experimental determination of the Eutectic
661 melting Curves in the systems Enstatite-Magnesite and Magnesite-Calcite from 15 – 80
662 GPa. Am Min doi:10.2138/am.2014.4735
663 Toby BH (2001) EXPGUI, a graphical user interface for GSAS. J App Cryst 34:210-213
664 Urlin VD (1966) Melting at ultra high pressures in a shock wave. Soviet Phys JETP 22:341
665 Weast RC, Astle MJ, Beyer WH (1985). Handbook of Chemistry and Physics. CRC Press Inc.,
666 Boca Raton, Florida.
667 Weingarten NS, Mattson WD, Rice BM (2009) Determination of the pressure dependent melting
668 temperatures of Al and Ni using MD. J App Phys 106:063524
669 Williams Q, Jeanloz R, Bass J, Svendsen B, Ahrens J (1987) The melting curve of iron to 250
670 gigapascals: A constraint on the temperature at Earth's centre. Science 236:181-182
671 Wu CJ, Söderlind P, Glosli JN, Klepeis JE (2009) Shear-induced anisotropic plastic flow from
672 body-centered-cubic tantalum before melting. Nature Mat 8:223-228
673 Yamazaki D, Ito E, Yoshino T, Yoneda A, Guo X, Zhang B, Sun W, Shimojoku A, Tsujino N,
674 Kunimoto T, Higo Y, Funakoshi K (2012) P-V-T equation of state for ε-iron up to 80 GPa
675 and 1900 K using the Kawai-type high Pressure apparatus equipped with sintered diamond
676 anvils. Geophys Res Lett 39:L20308
677 Zerr A, Boehler R (1994) Constraints on the melting temperature of the lower mantle from high-
678 pressure experiments on MgO and magnesiowüstite. Nature 371:506-508
679 Zhang W-J, Peng Y-F, Liu Z-L (2014a) Molecular dynamics study of melting curve, entropy of
680 fusion and solid–liquid interfacial energy of cobalt under pressure. Physica B 440:33-40
681 Zhang W-J, Liu Z-L, Peng Y-F (2014b) Molecular dynamics simulations of the melting curves and
682 nucleation of nickel under pressure. Physica B 449:144-149

683 Zhang X-L, Cai L-C, Chen J, Xu J-A, Jing F-Q (2008) Melting Behaviour of Mo by Shock Wave
684 Experiment. Chin Phys Lett 25:2969-2972

685 **Figure Captions**

686

687 **Figure 1:** Comparison between the phase diagrams of Fe and Ni up to 330 GPa based on selected
688 data from the literature. Thick lines and bold labels: the Fe phase diagram of Anzellini et al. (2013);
689 thin lines: Ni melting curves. Dashed lines indicate extrapolation. Experimental Ni melting curves
690 include that of Lazor et al. (1993; L93) and a curve fitted to the combined datasets of Errandonea et
691 al. (2013; 2001; E01) and Japel et al. (2005; J05). Curves based on MD simulations include those of
692 Bhattacharya et al. (2011; B11), Koči et al. (2006; K06), Pozzo & Alfè (2013; P&A13), Zhang et al.
693 (2014b; Z14) and Luo et al. (2010; L10). The MD simulations of Weingarten et al. (2009; W09)
694 only extend to 15 GPa and so are not shown separately for clarity, but match almost exactly the
695 melting curve of Pozzo & Alfè (2013). Closed triangles: shock melting points recalculated by Pozzo
696 & Alfè (2013) on the basis of the equations of state of liquid and solid Ni reported by Urlin et al.
697 (1966).

698

699 **Figure 2:** $P_{TH} = P_M - P_{300}$ plotted as a function of P_{300} for *in situ* experiments, where P_M is the
700 total pressure determined from the volume and temperature of the sample as measured during
701 melting and P_{300} is the pressure measured after quenching to room temperature. Closed symbols, Ni
702 with MgO as the pressure medium; Open symbols, KCl as the pressure medium with samples of
703 pure Ni (empty), $Ni_{91.6(4)}Si_{8.4(4)}$ (crosses) and $Ni_{95.8(2)}Si_{4.2(2)}$ (pluses). The data from the two Ni-Si
704 alloy compositions are from unpublished experiments in which the KCl pressure medium was also
705 used as the pressure standard. The lines are equally weighted linear regressions of the data with the
706 fit for KCl forced through zero to prevent negative thermal pressures at $P < 10$ GPa.

707

708 **Figure 3:** Ni melting data collected *in situ* at the ESRF (circles) and off-line at Bristol (squares).
709 For clarity, only the data corrected for the effects of thermal pressure P_{TH} are shown. See §2.5 of

710 the text for details of the correction procedure and Table 1 for the uncorrected values. The thick
711 black line is an equally weighted fit using the Simon-Glatzel equation while the grey field is a 2σ
712 error envelope. The thin black line is a similar fit to the uncorrected data (not shown). The red open
713 triangles represent the estimated temperature of the onset of rapid recrystallization in our *in situ*
714 experiments. The grey lines represent other Ni melting curves reported in the literature based on
715 experiments (thick) and MD simulations (thin) labelled as in Fig. 1, with dashed lines representing
716 extrapolation. Closed triangles: shock melting points recalculated by Pozzo & Alfè (2013) on the
717 basis of the equations of state of liquid and solid Ni reported by Urlin et al. (1966). The black cross
718 at 330 GPa represents the melting point of pure Fe based on the *in situ* experiments of Anzellini et
719 al. (2013). Experimentally determined melting curves for the MgO and KCl pressure media are
720 from Zerr & Boehler (1994) and Boehler et al. (1996) respectively.
721
722 **Figure 4:** *In situ* run 59A (Ni in MgO at $P_M = 45.8 \pm 1.3$ GPa). (a) Temperature vs. laser power
723 plot. The grey bar represents the melting temperature determined from the points within the melting
724 plateau (filled circles). The arrow represents the laser power at which LDS was first observed; LDS
725 was observed in all subsequent data above this power, which are colour coded as a function of laser
726 power. (b) XRD patterns colour coded to match (a). The black spectrum is the pattern collected
727 immediately before the onset of LDS; the dashed line is a fit to its background. Tick marks from top
728 to bottom represent Ni in the fcc structure and MgO. A constant intensity offset is applied to each
729 pattern such that all the patterns match at 2θ = 8°.
730
731 **Figure 5:** Le Bail fits (red lines) and difference curves (blue lines) of XRD data (black crosses)
732 from experiment 65A immediately before melting (a) and after temperature quench (b) and from
733 experiment 35A, also after quenching (c). Upper tick marks are for fcc-Ni; lower tick marks are for
734 MgO in (a) and (b) and for B2-KCl in (c). The arrows in (b) represent a quenched trace carbide

phase, probably with the Ni_3C stoichiometry. The single arrow in (c) indicates a reflection from the ruby pressure marker not included in the fit. See text for details.

Figure 6: Off-line run 77A (Ni in KCl at $P_M = 27.7 \pm 2.6$ GPa). (a) Temperature vs. laser power plot. Grey bar as in Fig. 4. Spectroradiometric measurements are represented by the circles (filled for the right-hand side, open for the left-hand side) while multispectral imaging radiometry measurements (made on the left-hand side only) are represented by the open squares. (b-j) Temperature maps determined by multispectral imaging radiometry measurements, colour coded as a function of temperature. The black circle in (b) represents the approximate location of the ~20 μm diameter incident laser beam while the grey bar in (d) represents the approximate location of the 3 μm wide aperture used for spectroradiometry. The letters b-j in (a) correspond to these temperature maps.

Figure 7: Off-line run 79B (Ni in MgO at $P_M = 125.1 \pm 2.6$ GPa). Symbols as in Fig. 5.

750 **Figure 1:**

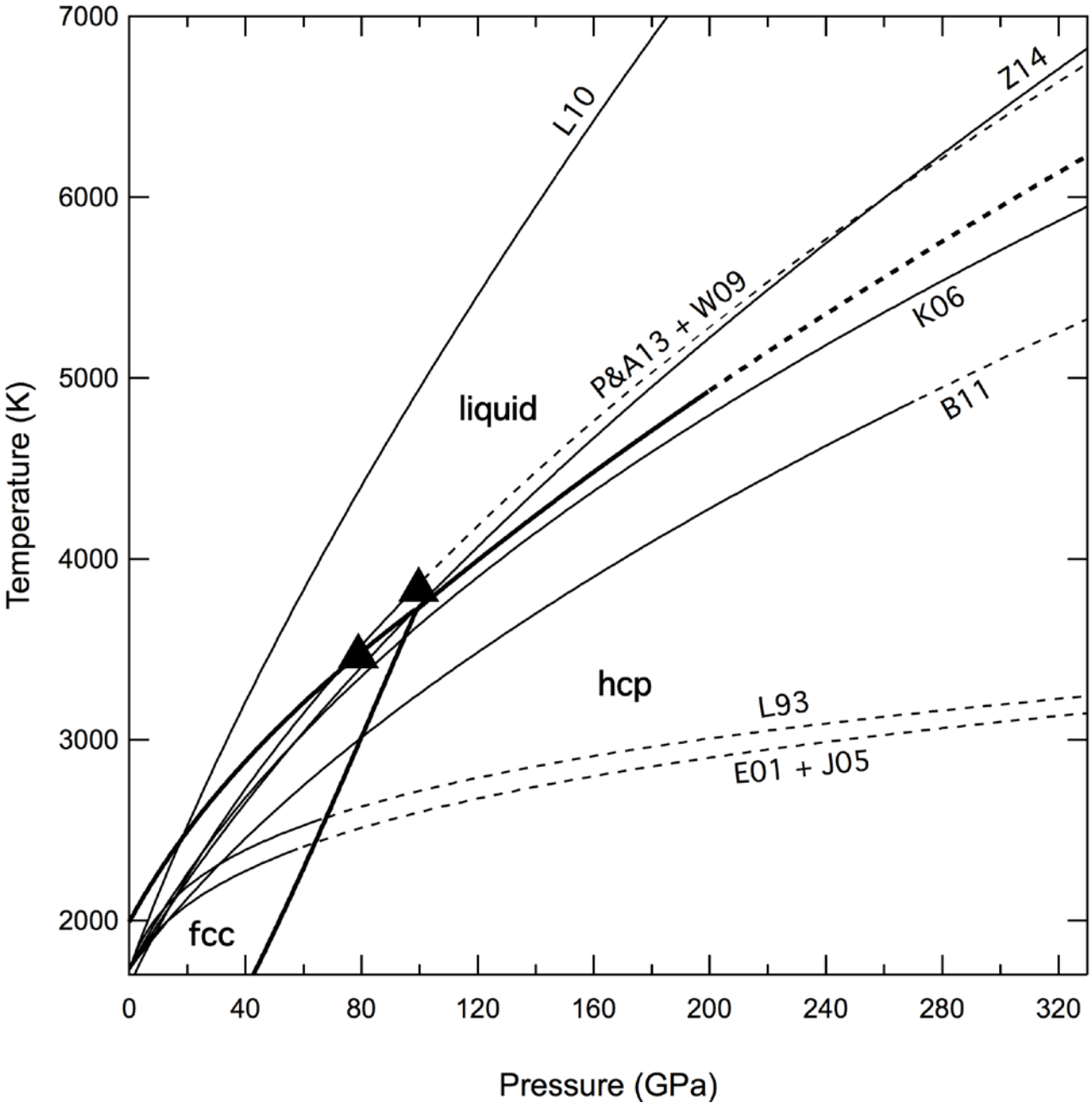

751

752

753 **Figure 2:**

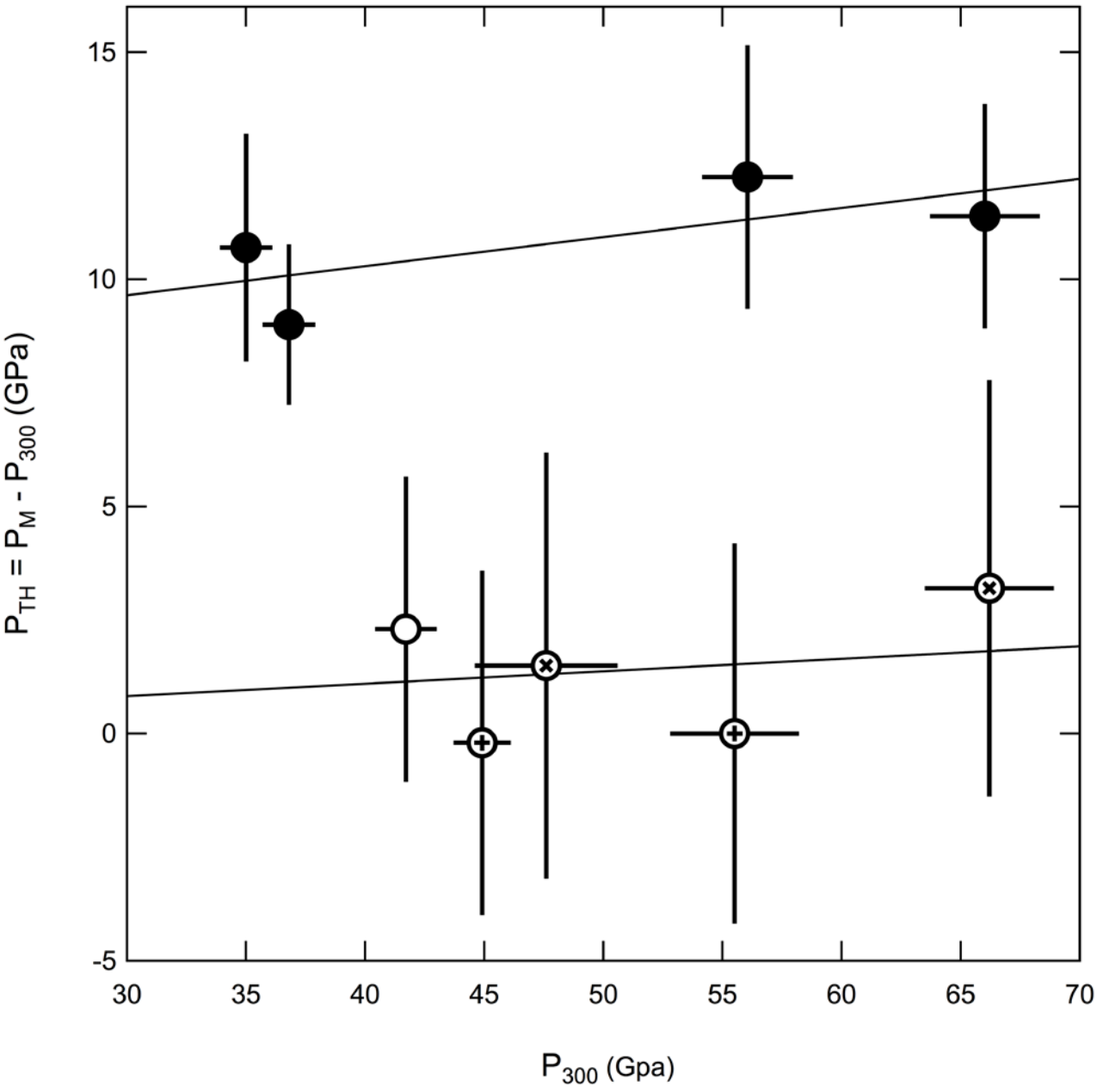

754

755

Figure 3:

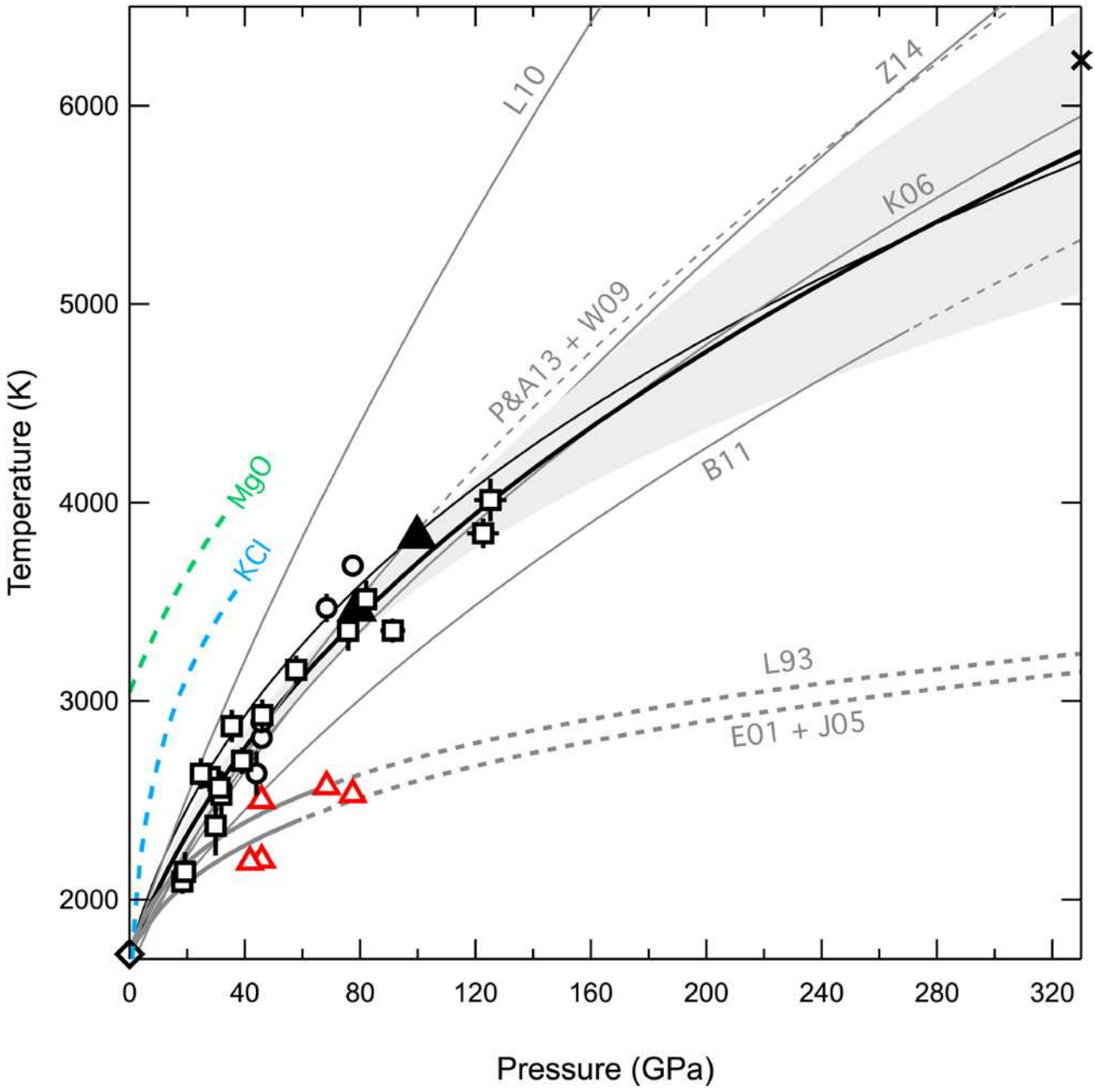
L10
Z14
K06
P&A13 + W09
B11
L93
E01 + J05
MgO
KCl
Temperature (K)
Pressure (GPa)
6000
5000
4000
3000
2000
0
40
80
120
160
200
240
280
320

Figure 4:

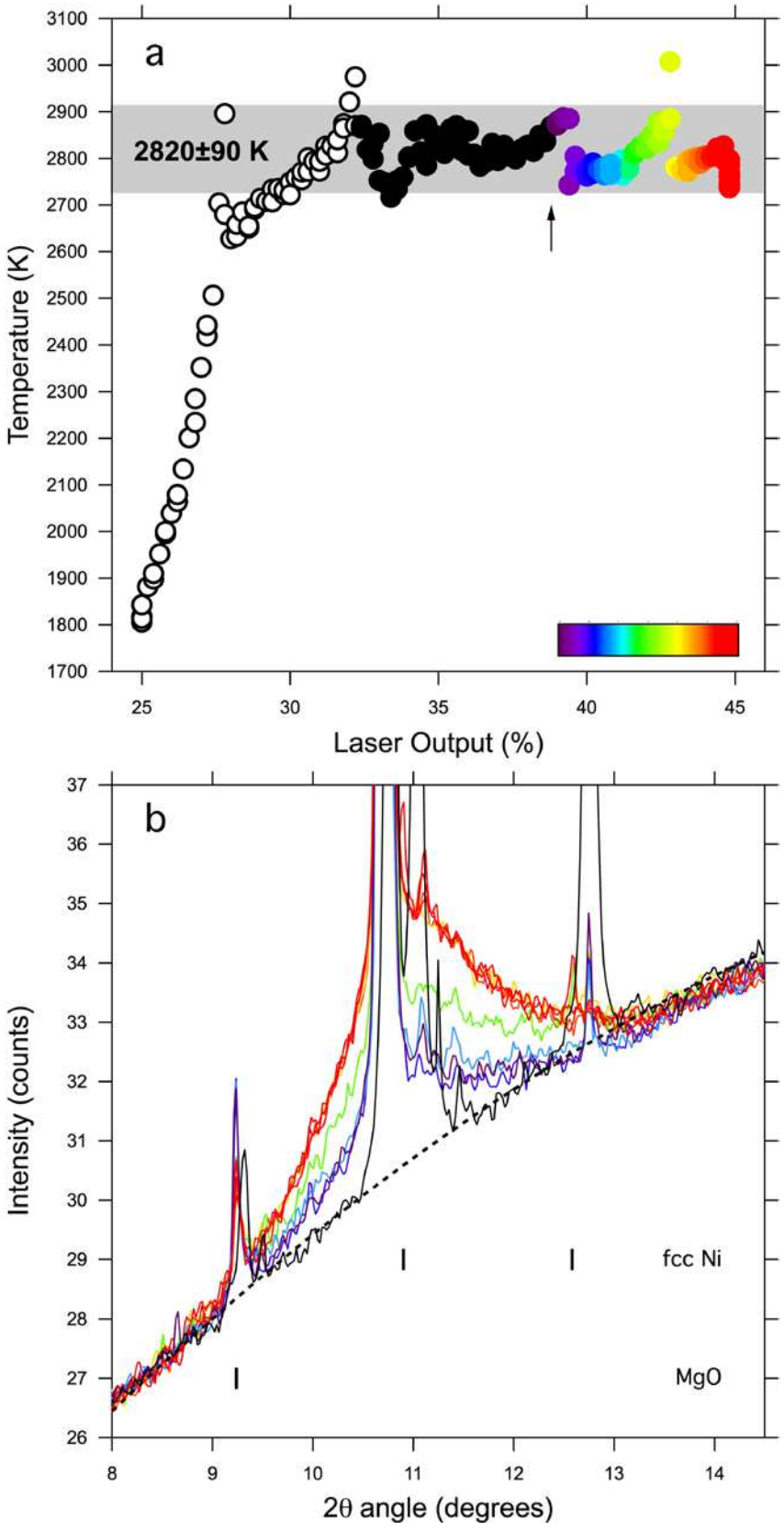
a
2820±90 K
Temperature (K)
Laser Output (%)
b
Intensity (counts)
fcc Ni
MgO
2θ angle (degrees)

762 **Figure 5:**

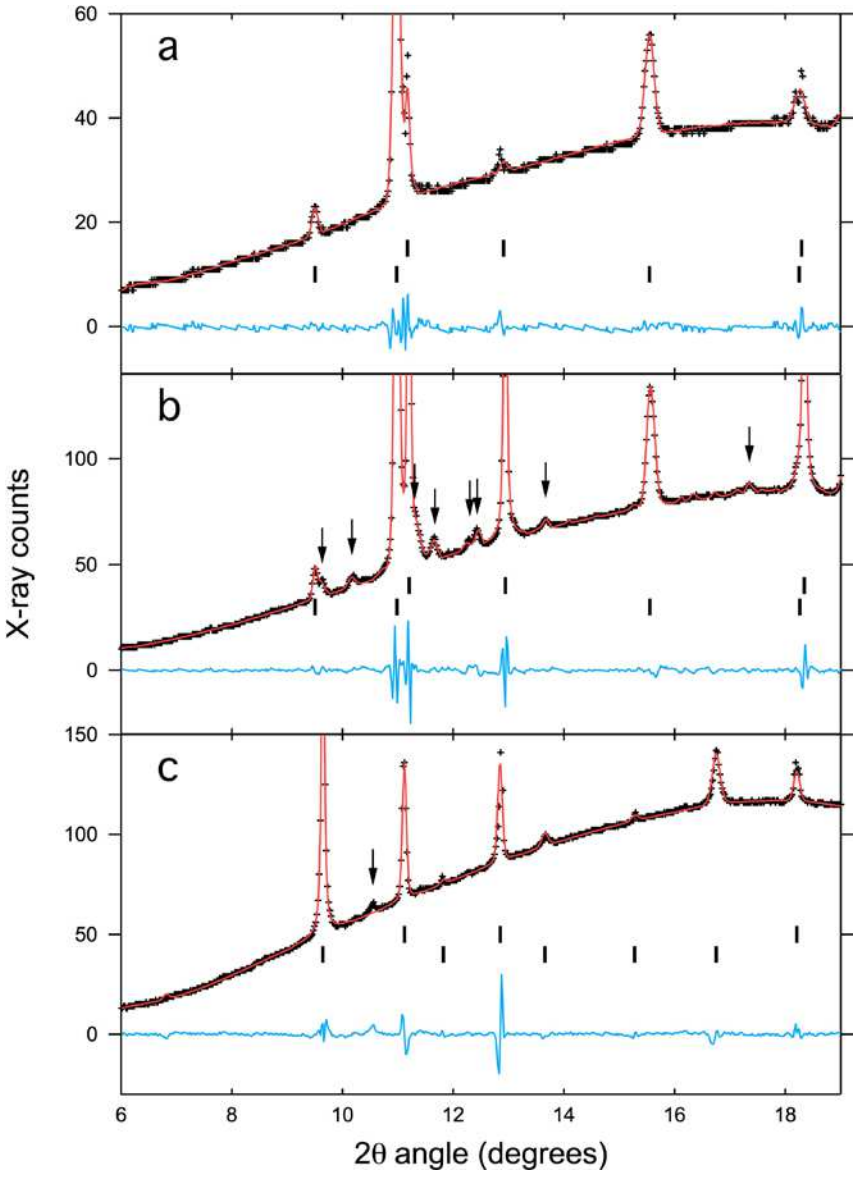

763

764 **Figure 6:**

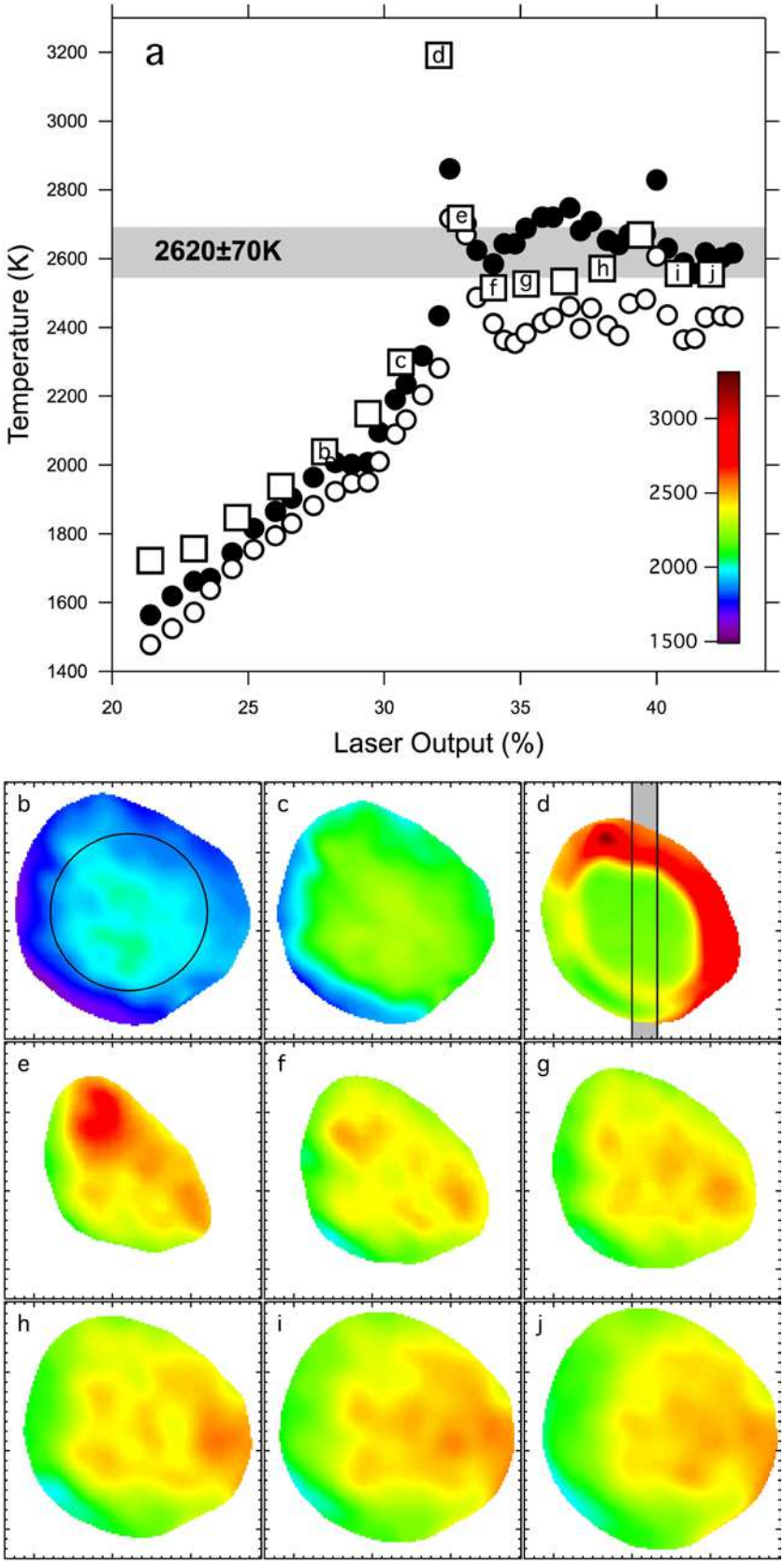

765
766

767 **Figure 7:**

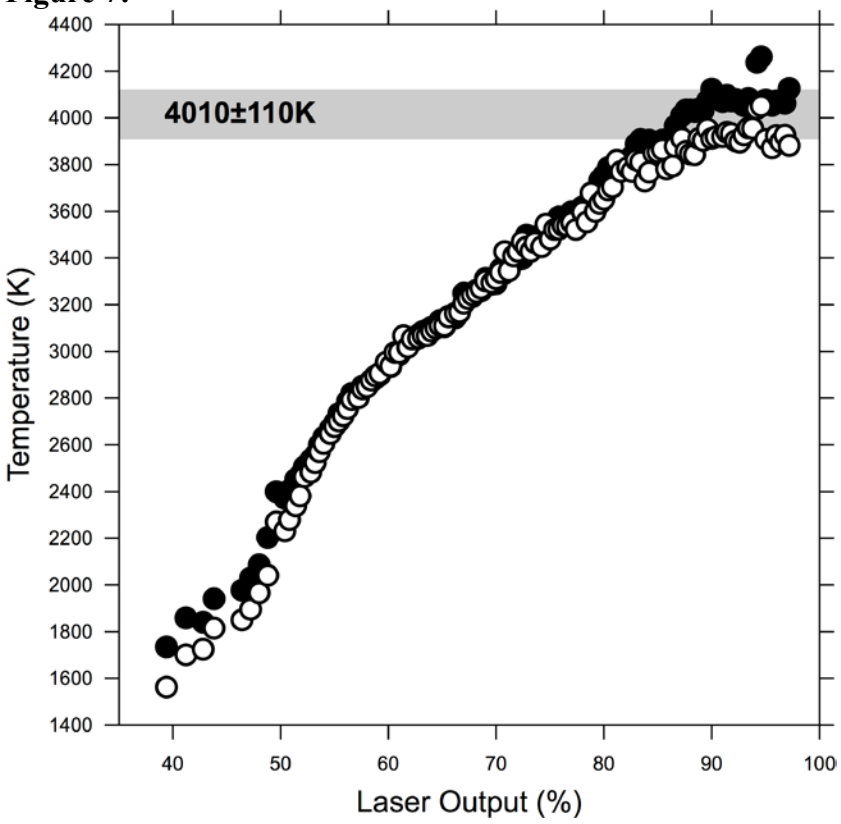

768
769

770

771 **Table 1:** Melting data

Code	Pressure medium	P_{300} (GPa)	P_M (GPa)	T_M (K)
76A	MgO	9.9±0.6	18.2±2.4	2091±59
76B	MgO	10.8±0.6	19.2±2.4	2140±96
70A	MgO	16±0.7	24.8±2.4	2635±75
77A	KCl	27±1	27.7±2.6	2618±70
42A	KCl	29±1	29.8±2.7	2372±146
71A	MgO	22±0.9	31.1±2.5	2564±24
42B	KCl	31±1	31.9±2.7	2529±117
70B	MgO	26±1	35.4±2.6	2874±78
77B	KCl	38±1.2	39.0±2.9	2700±66
35A	**KCl**	41.7±1.3	**44.0±2.7**	**2636±107**
59B	**MgO**	35±1.1	**45.7±1.8**	**2894±83**
59A	**MgO**	36.8±1.1	**45.8±0.9**	**2816±44**
70C	MgO	36±1.2	46.0±2.8	2930±76
71B	MgO	47±1.5	57.7±3.2	3159±66
65A	**MgO**	56.1±1.9	**68.3±2.4**	**3470±69**
71C	MgO	64±2.2	75.8±3.7	3354±97
65B	**MgO**	66±2.2	**77.4±1.9**	**3683±37**
75A	MgO	69.8±2.3	82.0±4.0	3514±91
75B	MgO	78.5±2.6	91.3±4.3	3356±58
79A	MgO	108±3.4	122.6±5.5	3846±72
79B	MgO	110.4±3.5	125.1±5.6	4014±104

Data in bold were collected *in situ*

772